Supplementary Information

Mechanistic insights of the ultralow wear and low friction of carbon fiber reinforced PTFE in trace moisture environment

Pontus Johansson[1]*, Robin Elo[2], Vahid Fadaei Naeini[1], Pär Marklund[1], Marcus Björling[1], Yijun Shi[1]

[1]Division of Machine Element, Luleå University of Technology, Luleå SE-97187, Sweden

[2]Ångström Tribomaterials Group, Department of Engineering Sciences, Uppsala University, Sweden

*Corresponding author. E-mail: pontus.johansson@ltu.se

Contents

1. EDS of steel-tribofilm
2. Nanoindentation of steel-tribofilm
3. ATR-FTIR of steel-tribofilm
4. Raman of graphite surface
5. MD simulation

1. EDS of steel-tribofilm

EDS results of the steel-tribofilm are shown in Fig. S1. The EDS measurement was made on a region with thicker tribofilm, typically found around the center of the wear track. The thicker tribofilm region was chosen to increase the signal from the tribofilm compared to the underlying steel surface. Note that the FIB-TEM analysis was made from a region with thinner tribofilm which better represents the whole wear track. The areas with thicker tribofilm, as indicated by the darker gray in the electron image, Fig. S1, shows high relative intensity of fluorine, iron and chromium. This indicates that chromium fluoride may also exist in the tribofilm together with iron (II) fluoride, which was confirmed by TEM.

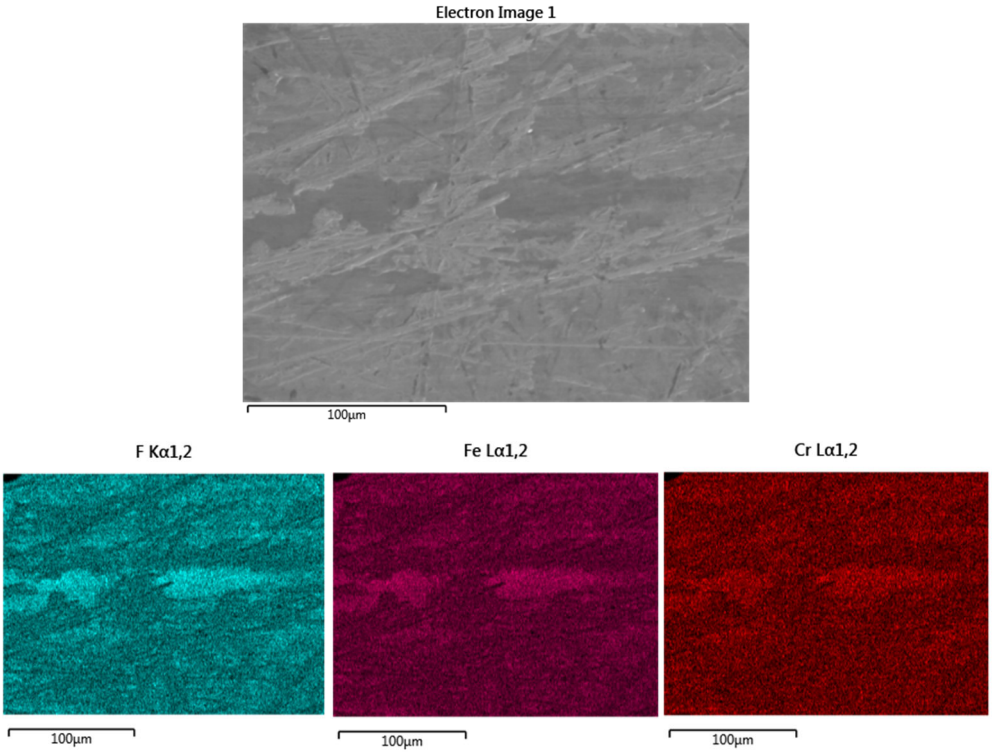

Fig. S1 *Secondary electron image and related EDS map of fluorine (F), iron (Fe) and chromium (Cr) taken on region of the steel counterface with thick tribofilm*

2. Nanoindentation of steel-tribofilm

Nanoindentations were made on the steel-tribofilm and on the steel counterface outside the wear track. Indentations were made on tribofilm regions that appeared thick and thin according to the microscope used for the positioning of the indentations. To minimize influence on the results from the substrate, low contact depths were needed. From preliminary indentations, the contact loads 0.1 and 0.3 mN were chosen. 24 indentations were made in total, 8 per surface region and 4 per load. The indentation results, Fig. S2, indicate that the steel-tribofilm, that mainly consists of iron (II) fluoride, have a hardness of about 3 to 5 GPa. This is relatively hard, even though the hardened steel substrate seems to be harder. However, more indentations would be needed to provide quantitative values for the hardness.

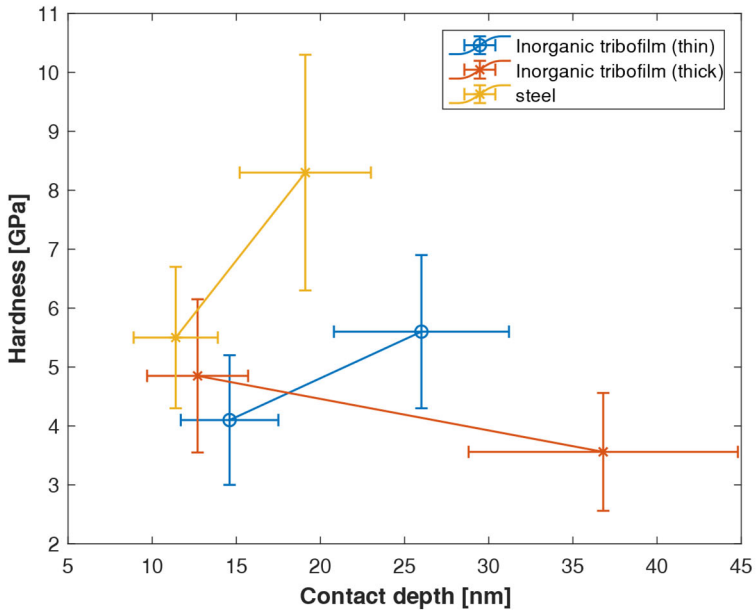

Fig. S2 Average hardness and contact depths from nanoindentations at 0.1 and 0.3 mN contact loads of the inorganic tribofilm and the original steel counterface. Error bars indicate the standard deviation

3. ATR-FTIR of steel-tribofilm

A typical ATR-FTIR spectrum of the steel-tribofilm is shown in Fig. S3. The spectrum clearly lacks the characteristic peaks at 1150 and 1205 cm^{-1} for PTFE [1]. The main peak at 500 cm^{-1} can be attributed to the Fe-F bond in the iron fluoride [2]. The weak and broad peak at 3500 to 3000 cm^{-1} can be assigned to the stretching vibration of hydroxyl groups (O-H) [3] and could possibly be due to adsorbed moisture on the tribofilm surface.

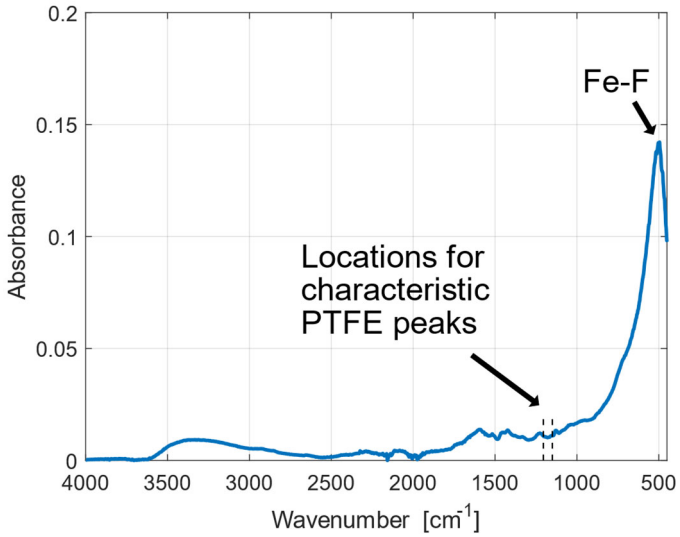

Fig. S3 ATR-FTIR spectrum of the inorganic tribofilm formed on the steel counterface

4. Raman of graphite surface

Raman measurements were taken on the graphite surface before and after sliding against the steel-tribofilm at mild sliding conditions (μ~0.08), see Fig. S4. The increase in the D/G ratio after sliding indicate an increased disorder of the material, i.e. the carbon in the surface have become more turbostratic and less graphitic [4].

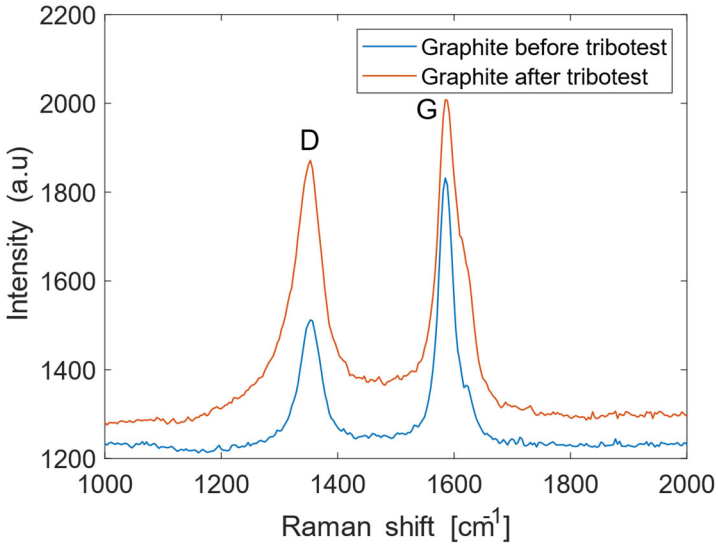

Fig. S4 *Raman spectra of the sliding surface of a graphite sample before after tribotest against the inorganic tribofilm in dry nitrogen at mild sliding conditions*

5. MD simulation

5.1 Molecular configuration of the system and simulation details

Molecular dynamics (MD) simulation offers a dependable computational framework for assessing the tribochemistry of lubrication systems and examining the interfacial properties on a molecular scale. In the first stage of preparing the molecular model for MD simulation, the crystallographic structure of the iron fluoride (FeF_2) unit cell [5], [6] was expanded using VESTA 3.5.0 [7] to build a 10×10×3 supercell with dimensions of 49.3×49.3×13.59 $Å^3$ (Fig. ***S5***, Panels a, b, and c). Later, the equilibrated structure of carbon fiber including 99.5% wt carbon (As revealed in Fig. ***S5***5, Panels d and e), which is the output product of a research carried out by Vuković et al. [8], was inserted on the supercell of iron fluoride using Packmol [9].

In order to express the interaction of iron and fluorine atoms in iron fluoride, a third-generation of charge-optimized many-body (COMB) potentials [10], entitled COMB3, was utilized. The COMB formalism incorporates concepts such as bond order and varying ionic charges to create a versatile description of all three types of bonding at the atomic level [11]–[13]. The third-generation incorporates minor modifications to the functional form to enhance its flexibility in modeling diverse bonding scenarios, and a significant expansion of the coordination function to capture the complex bonding environments present in carbon-based compounds more accurately. The COMB3 potential can be generally expressed as the following:

$$U_{Tot.} = U_{Elec.}(q, r) + U_{Short}(q, r) + U_{vdW}(r) + U_{Corr.}(i, j, k) \quad \text{Eqn. 1}$$

In Eqn. 1, the potential energy ($U_{Tot.}$) is determined by adding the contributions of the electrostatic energy ($U_{Elec.}$), the short-range energy (U_{Short}), the long-range van der Waals energy (U_{vdW}), and a correction term ($U_{Corr.}$). The electrostatic energy can be expressed as follows:

$$U_{Elec.}(q, r) = U_q(q, r) + U_{qq}(q, r) + U_{qZ}(q, r) + U_{Polar}(q, r) \quad \text{Eqn. 2}$$

The electrostatic energy encompasses four energy contributions, namely, the energy required to form a charge from a neutral atom (U_q), the interactions between charges (U_{qq}), the interactions between charges and atomic nuclei (U_{qZ}), and the energy related to polarizability (U_{Polar}). The required energy to form a charge (U_q) considers various factors such as electron affinity, ionization energies, and field effects such as changes in electronegativity and chemical hardness with respect to the bonding environment [14]. The specific potential parameters for iron and fluorine species in COMB3, which were determined by Tangarife et al. [15], were utilized. Moreover, the interatomic interactions between carbon and hydrogen in carbon fiber were computed utilizing the adaptive intermolecular reactive bond order (AIREBO) potential [16]. The implemented modifications in AIREBO potential involve adjustments to both the repulsive and attractive pair interaction functions to accurately capture bond properties, as well as the incorporation of long-range atomic interactions and single bond torsional interactions. The van der Waals interaction parameters corresponding to Fe, F, C, and H were derived from references [17],

[18], [19], and [20], respectively. The Lorentz-Berthelot combining rules [21], [22] were utilized to derive the parameters governing the van der Waals interactions within the interface region, including Fe-C, Fe-H, F-C, and F-H. The atomic interactions in the system were ultimately characterized using the COMB3, AIREBO, and Lennard-Jones potentials.

The LAMMPS package [23] was utilized to carry out all MD simulation steps, with a timestep of 0.25 fs. By utilizing the LAMMPS simulation package, it is feasible to simultaneously employ multiple potentials in a hybrid manner during a simulation. The MD simulations was executed in three distinct phases. In the first stage, the temperature of the system was gradually elevated from T = 298.15 K to T=353.15 K under the NVT ensemble. Subsequently, the system was subjected to equilibration under the NVT ensemble at T= 353 K, facilitated by the Nose-Hoover thermostat . During the third and final stage, a force was applied to the atoms present in the outer layers of the system, generating a normal stress in the Z direction (Fig. S5, Panel f). In this stage, four series of simulations were performed independently to apply σ=2, 20, 100, and 200 MPa as the normal stress to the system. Simultaneously, this group of atoms is pulled along the X-axis in opposing directions to one another, with a consistent velocity of V = 0.75 m/s. The simulation time for step is presented in Table S1.

Table S1. Simulation steps together with simulation time

Procedure	Time/ns
Raising Temperature from T=25 ˚C to T=80 ˚C	0.1
Equilibration at T=80 ˚C	0.1
SMD simulation (Applying normal stress and shear strain)	1

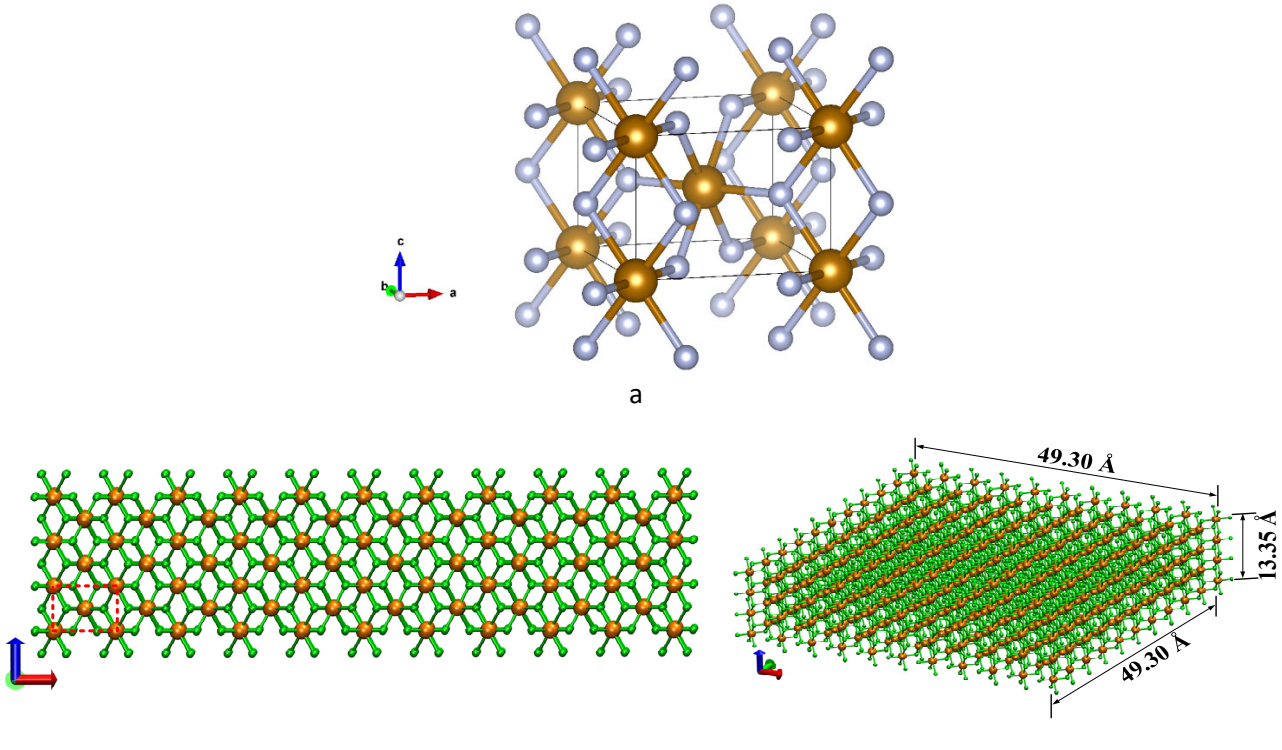

a

b

c

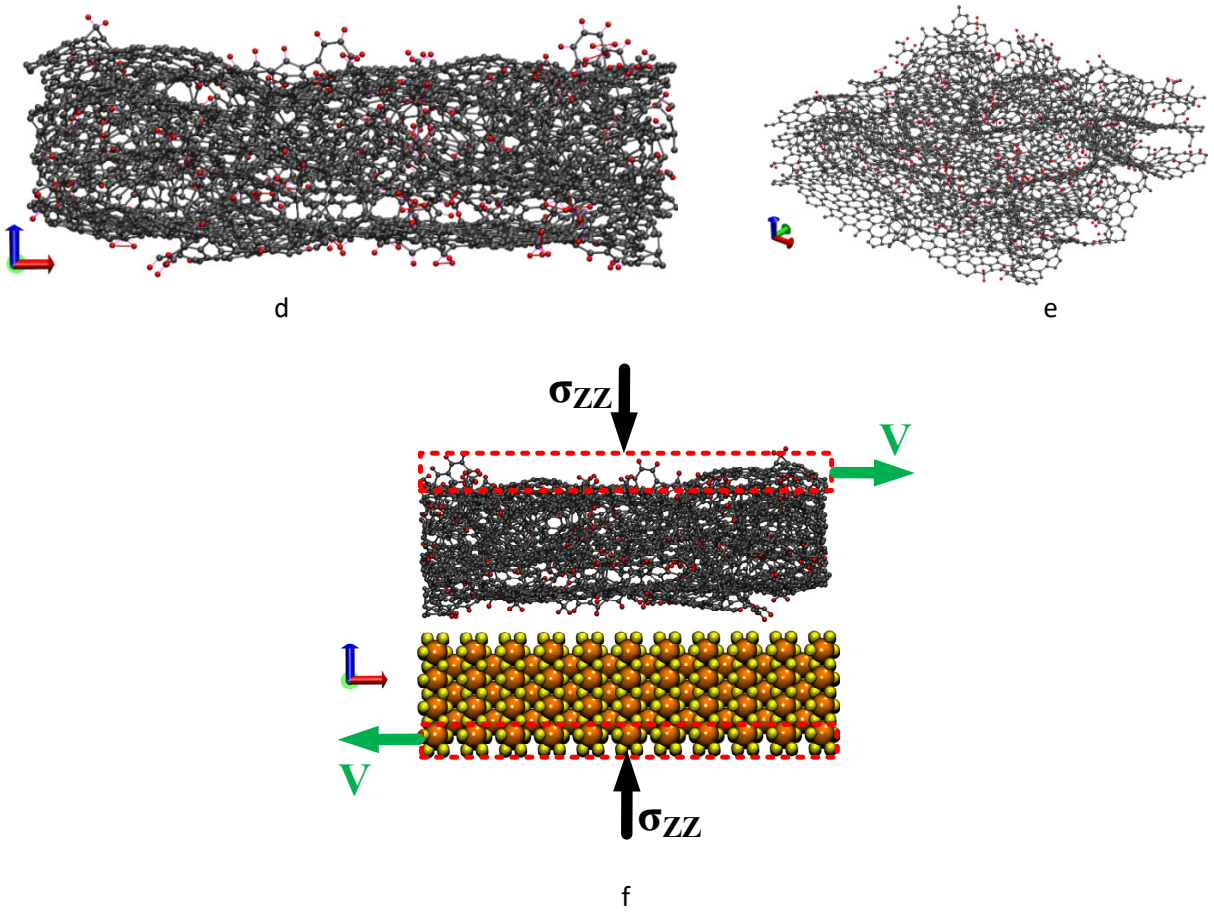

Fig. S5 *The process of building the molecular configuration of the system. a. The unit cell of FeF_2 [5], [6], b. The sideview of the crystal structure of a 10×10×3 supercell of FeF_2. The boundaries of the unit cell are shown by red box. built and rendered by VESTA version 3.5.0 [7], c. Crystal structure of a 10×10×3 supercell of FeF_2 together with the dimensions (3D view), d and e. Molecular structure of the Carbon fiber (Side view and 3D view) [8], f. The initial configuration of the simulation system. The snapshots in panels b-f have been rendered by VMD [24]*

5.2 Results and discussion

In this section, the results associated with the MD simulation of the tribological performance of carbon fiber against iron fluoride is presented.

5.2.1 System temperature

As the first output of the MD simulation, the time evolution of the system temperature during different stages is illustrated in Fig. S6. The system temperature increases almost linearly in the first stage and oscillates around the constant value of T=353 K in the second and third stages. The thermostat stabilized the system temperature during the second and third stages, as highlighted by Fig. S6.

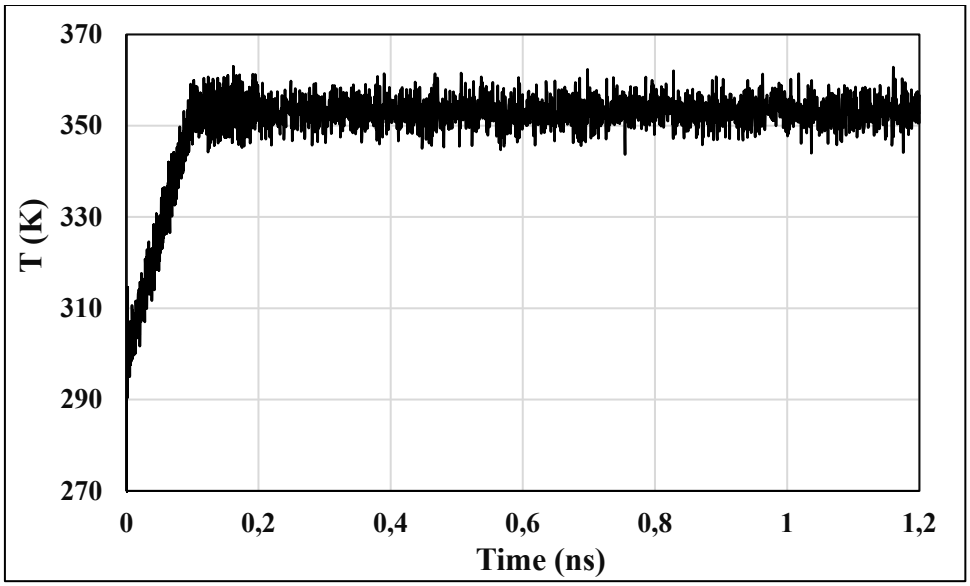

Fig. S6 *Time evolution of the system temperature*

5.2.2 Radial distribution function and stacking

To accomplish an investigation of the distribution of carbon atoms within the carbon fiber during the MD simulation, we calculated the radial distribution function (RDF) of carbon atoms. In the layered structure of graphite, the carbon-carbon covalent bond length measures approximately 1.42 Å. Applying normal stress and shear strain to multi-layer hexagonal carbon fiber structures resulted in crystallographic defects, including Stone-Wales defects [25]. However, despite these defects, hexagonal structures mostly maintained their original arrangement. Furthermore, the formed pyracyclene rearrangement exhibited slight variations in the carbon-carbon bond length compared to the intact arrangement. Consequently, the distance between the nearest carbon neighbors (blue-colored carbons in Fig. S7b and c is slightly greater (0.03 Å) than the one in the defectless graphene layers. According to Fig. S7a, it is inferred that the frequency of the first neighbors remains significantly higher compared to the second and third ones, which indicates that a substantial portion of the carbon-carbon covalent bonds has been retained within the layers of carbon fiber.

Naturally, when the structural defects arise in carbon fiber, the distance between the second carbon neighbors (the green-colored carbons in Fig. S7b and c undergoes minimal alteration in comparison to a defectless graphene layer. As depicted in Fig. S77a, the position of the second peak in the RDF diagram slightly exceeds the geometric distance of the second neighbors in Fig. S7c.

By subjecting the system to normal stress of up to 200 MPa, a significant influence on the stacking space within the multiple layers of carbon fiber is anticipated. However, an analysis of the third neighbors in the RDF diagram reveals that the third neighbors of carbon (depicted as yellow-colored carbons in Fig. S7b and c are positioned at r=3.65 Å, which is 0.3 Å greater than the equilibrium distance of defectless graphite layers. It should be noted that an intrinsic planar disorder exists between consecutive layers in the carbon fiber structure, and the location of the third neighbors in the

defectless graphite structure is also approximately 3.65 Å. The presence of the third peak in the RDF diagram confirms that, despite the application of normal stress and some of local planar distortions, the successive layers of carbon fiber retain their original stacking space to a considerable extent. These findings align with the experimental observations in this context.

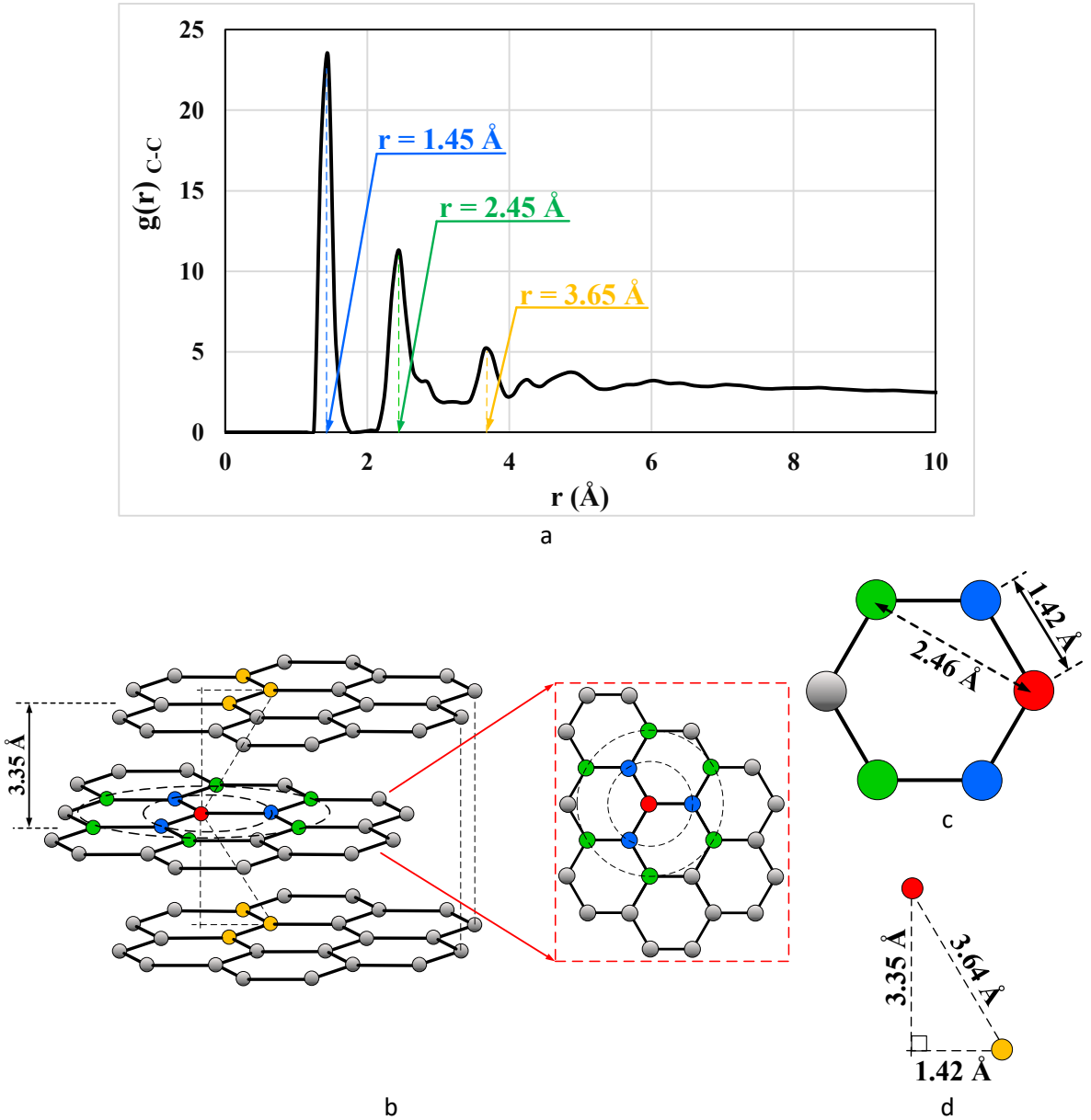

Fig. S7 *a) The radial distribution function of the carbon atoms within the carbon fiber. b) The stacking arrangement of layers of carbon atoms in graphite. c) The geometrical distances of the fisrt and second nearest neighbors around carbon (shown in blue and green, respectively). d) The geometrical distances of the third nearest neighbors around carbon (shown in yellow)*

5.2.3 Pulling force and friction coefficient

Fig. S8 depicts the time evolution diagram of the shear force, required to apply the shear deformation in the systems of study. As illustrated in Fig. S8, for all instances within the initial 0.1 ns, augmenting the normal force applied on the outer layers of the system results in an initial rise followed by a rapid decline in the shear force, which subsequently oscillates around a specific value. The initial elevation of the shear force is directly proportional to the normal stress applied to the system. Furthermore, as

the normal stress increases, the magnitude of fluctuations in the shear force amplifies. A clearer depiction of the shear force fluctuations during the final 0.2 ns is presented in the inset of Fig. S8.

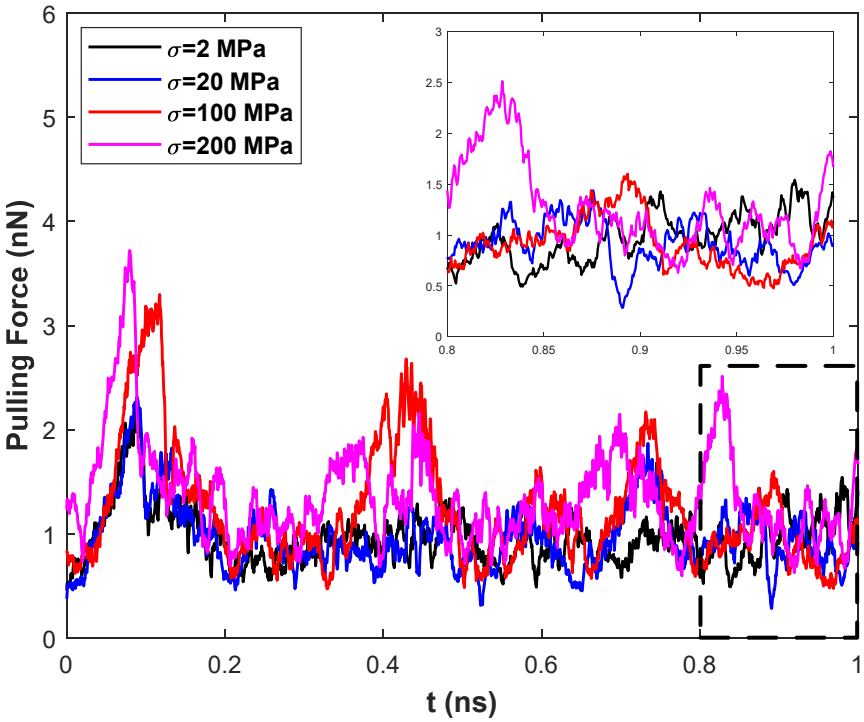

Fig. S8 *The time variation of shear force in the systems of study*

Fig. S9 demonstrates the correlation between the shear stress and the normal stress by examining the average shear force during the final 0.2 ns of each simulation. The results reveal a linear increase in the average shear stress as the normal stress escalates, albeit with a distinct offset. To determine the friction coefficient of the system, a linear equation proposed by Amentons-Coulomb and expanded by Derjaguin [26] is employed. The linear expression, $\tau_{xy}= \mu\sigma_{zz}+ \tau_0$, incorporates the Derjaguin intercept (τ_0), which depends on the adhesion at the sliding surfaces. By a linear fit of the shear stress data, the friction coefficient, μ, can be accurately derived. In this regard, the coefficient of friction between carbon fiber and iron fluoride is determined to be 0.0602.

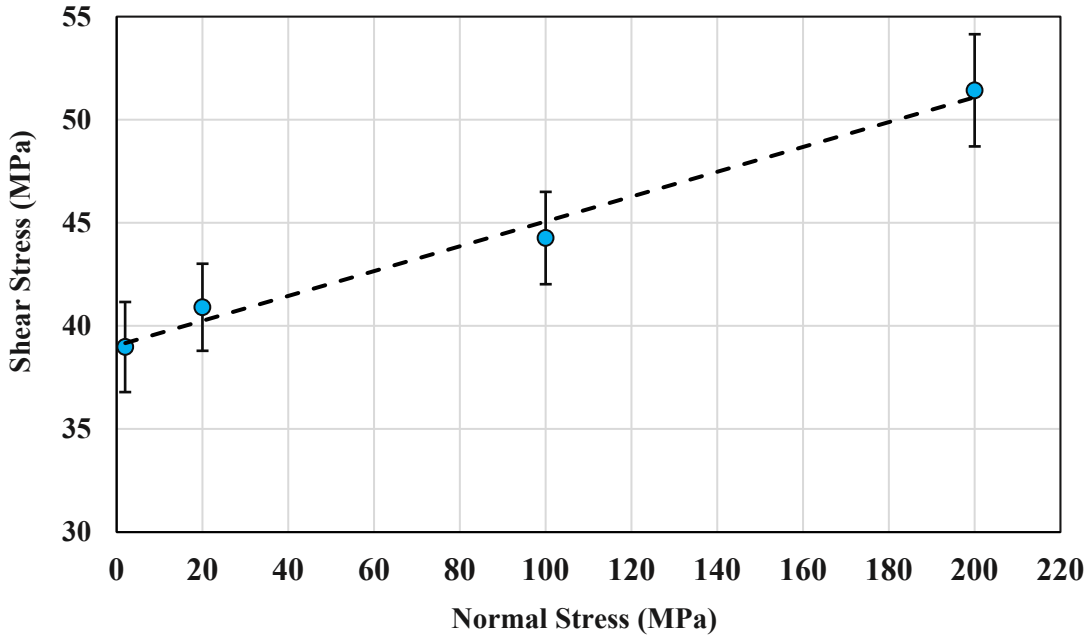

Fig. S9 *Variation in mean shear stress with normal stress for carbon fiber on iron fluoride. Dashed lines are linear fitting to Amontons-Coulomb friction expression modified by Derjaguin [22]*

5.2.4 Surface interaction energy

The time-dependent alterations in the surface interaction energy with the carbon fiber are presented in Fig. The inset of provides a more distinct representation of the fluctuations in non-bonded interaction energy observed in the last 0.2 ns of simulations. Upon initiation of the simulation and the placement of carbon fiber on the iron fluoride substrate, the attractive non-bonded interaction energy between the fiber and substrate promptly reaches around 25 eV, and it fluctuates around this energy level throughout the equilibration stage. As anticipated, the application of mechanical stress on the system promptly amplifies the attractive interaction energy, in direct proportion to the applied stress. Moreover, it appears that higher levels of normal stress prompt larger jumps in the interaction energy, aligning with the shear stress outcomes presented in the preceding section. Particularly, the amounts of attractive interaction energy at σ=20 MPa and σ=100 MPa exhibit minimal disparity, a characteristic that is also reflected in the calculated shear stress for these particular cases. To compare the interaction energy with other conventional substrates, an identical structure of carbon fiber was placed on the crystal surface of magnetite, with the same dimensions as the iron fluoride surface. The attractive interaction energy between the magnetite surface and carbon fiber was observed to be more than double that of the iron fluoride scenario.

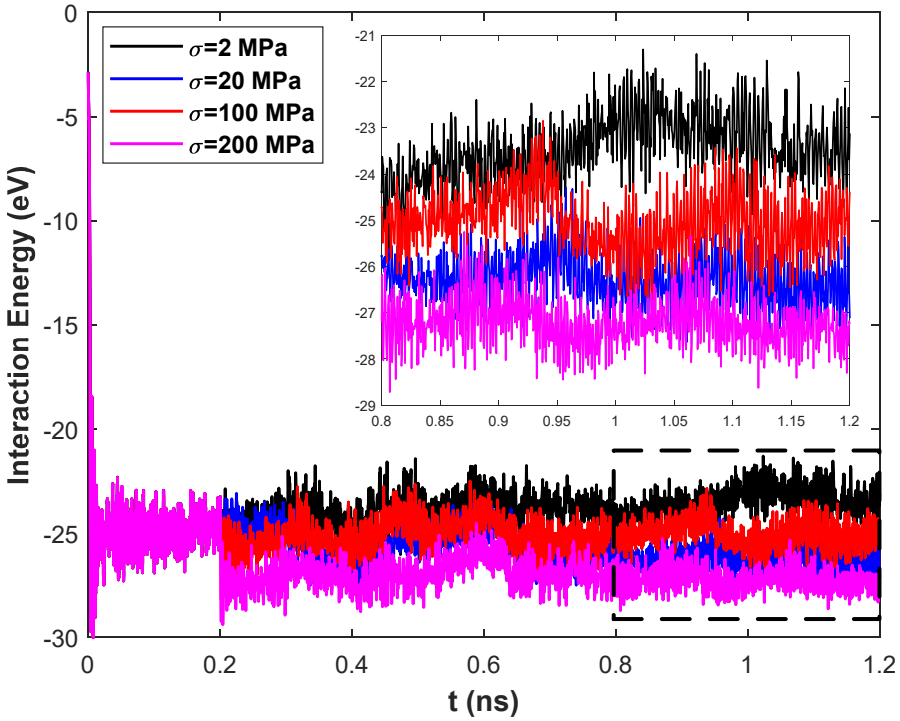

Fig. S10 *Time evolution of the non-bonded interaction egergy between the iron fluoride surface and the carbon fiber*

References

[1] Piwowarczyk J, Jedrzejewski R, Moszyński D, Kwiatkowski K, Niemczyk A, Baranowska J. XPS and FTIR studies of polytetrafluoroethylene thin films obtained by physical methods. Polymers 2019;11. https://doi.org/10.3390/polym11101629.

[2] Blower PJ, Levason W, Luthra SK, McRobbie G, Monzittu FM, Mules TO, et al. Exploring transition metal fluoride chelates – synthesis, properties and prospects towards potential PET probes. Dalton Transactions 2019;48:6767–76. https://doi.org/10.1039/C8DT03696A.

[3] Przedlacki M, Kajdas C. Tribochemistry of fluorinated fluids hydroxyl groups on steel and aluminum surfaces. Tribology Transactions 2006;49:202–14. https://doi.org/10.1080/05698190500544676.

[4] Schuepfer DB, Badaczewski F, Guerra-Castro JM, Hofmann DM, Heiliger C, Smarsly B, et al. Assessing the structural properties of graphitic and non-graphitic carbons by Raman spectroscopy. Carbon 2020;161:359–72. https://doi.org/10.1016/j.carbon.2019.12.094.

[5] J. W. Stout and S. A. Reed, "The crystal structure of mnf2, fef2, cof2, nif2 and znf2," *J. Am. Chem. Soc.*, vol. 76, no. 21, pp. 5279–5281, 1954.

[6] "Materials Project." https://materialsproject.org/materials/mp-556911 (accessed May 11, 2023).

[7] K. Momma and F. Izumi, "VESTA 3 for three-dimensional visualization of crystal, volumetric and morphology data," *J. Appl. Crystallogr.*, vol. 44, no. 6, pp. 1272–1276, 2011.

[8] F. Vuković and T. R. Walsh, "Practical atomistic models of carbon fiber surfaces with tuneable topology and topography," *Compos. Sci. Technol.*, vol. 216, p. 109049, 2021.

[9] L. Martínez, R. Andrade, E. G. Birgin, and J. M. Martínez, "PACKMOL: a package for building initial configurations for molecular dynamics simulations," *J. Comput. Chem.*, vol. 30,

no. 13, pp. 2157–2164, 2009.

[10] T. Liang, B. Devine, S. R. Phillpot, and S. B. Sinnott, “Variable charge reactive potential for hydrocarbons to simulate organic-copper interactions,” *J. Phys. Chem. A*, vol. 116, no. 30, pp. 7976–7991, 2012.

[11] T. Liang *et al.*, “Classical atomistic simulations of surfaces and heterogeneous interfaces with the charge-optimized many body (COMB) potentials,” *Mater. Sci. Eng. R Reports*, vol. 74, no. 9, pp. 255–279, 2013.

[12] T. Liang *et al.*, “Reactive potentials for advanced atomistic simulations,” *Annu. Rev. Mater. Res.*, vol. 43, pp. 109–129, 2013.

[13] Y. K. Shin *et al.*, “Variable charge many-body interatomic potentials,” *MRS Bull.*, vol. 37, no. 5, pp. 504–512, 2012.

[14] H. Toufar *et al.*, “Dependence of the hardness of atoms in molecules on the local environment: An ab initio study,” *J. Phys. Chem.*, vol. 100, no. 38, pp. 15383–15387, 1996.

[15] E. Tangarife, A. H. Romero, and J. Mejía-López, “A charge optimized many-body potential for iron/iron-fluoride systems,” *Phys. Chem. Chem. Phys.*, vol. 21, no. 36, pp. 20118–20131, 2019.

[16] S. J. Stuart, A. B. Tutein, and J. A. Harrison, “A reactive potential for hydrocarbons with intermolecular interactions,” *J. Chem. Phys.*, vol. 112, no. 14, pp. 6472–6486, 2000, doi: 10.1063/1.481208.

[17] D. Savio, N. Fillot, P. Vergne, and M. Zaccheddu, “A model for wall slip prediction of confined n-alkanes: effect of wall-fluid interaction versus fluid resistance,” *Tribol. Lett.*, vol. 46, pp. 11–22, 2012.

[18] S. H. Lee and J. C. Rasaiah, “Molecular dynamics simulation of ion mobility. 2. Alkali metal and halide ions using the SPC/E model for water at 25 C,” *J. Phys. Chem.*, vol. 100, no. 4, pp. 1420–1425, 1996.

[19] Y. Y. Zhang, C. M. Wang, Y. Cheng, and Y. Xiang, “Mechanical properties of bilayer graphene sheets coupled by sp3 bonding,” *Carbon N. Y.*, vol. 49, no. 13, pp. 4511–4517, 2011.

[20] P. André, L. Brunet, W. Bussiere, J. Caillard, J. M. Lombard, and J. P. Picard, “Transport coefficients of plasmas consisting of insulator vapours: Application to PE, POM, PMMA PA66 and PC,” *Eur. Phys. Journal-Applied Phys.*, vol. 25, no. 3, pp. 169–182, 2004.

[21] H. A. Lorentz, “Ueber die Anwendung des Satzes vom Virial in der kinetischen Theorie der Gase,” *Ann. Phys.*, vol. 248, no. 1, pp. 127–136, 1881.

[22] D. Berthelot, “Sur le mélange des gaz,” *Compt. Rendus*, vol. 126, no. 3, p. 15, 1898.

[23] A. P. Thompson *et al.*, “LAMMPS-a flexible simulation tool for particle-based materials modeling at the atomic, meso, and continuum scales,” *Comput. Phys. Commun.*, vol. 271, p. 108171, 2022.

[24] W. Humphrey, A. Dalke, and K. Schulten, “VMD: Visual molecular dynamics,” *J. Mol. Graph.*, vol. 14, no. 1, pp. 33–38, 1996, doi: 10.1016/0263-7855(96)00018-5.

[25] A. J. Stone and D. J. Wales, “Theoretical studies of icosahedral C60 and some related species,” *Chem. Phys. Lett.*, vol. 128, no. 5–6, pp. 501–503, 1986.

[26] S. J. Eder, A. Vernes, and G. Betz, “On the Derjaguin offset in boundary-lubricated nanotribological systems,” *Langmuir*, vol. 29, no. 45, pp. 13760–13772, 2013.